Volume 1 | Number 1 | Jan 2013 | Pages 1–100

Journal of
Materials Chemistry A

Materials for energy and sustainability
www.rsc.org/materialsA

Li⁺

ROYAL SOCIETY
OF CHEMISTRY

ROYAL SOCIETY
OF CHEMISTRY

www.rsc.org/materialsA

Systematic comparison of different dopants in thin film hematite (α-Fe$_2$O$_3$) photoanodes for solar water splitting

Kirtiman Deo Malviya, Hen Dotan, Dmitry Shlenkevich, Anton Tsyganok, Hadar Mor, Avner Rothschild*

Department of Materials Science and Engineering, Technion- Israel Institute of Technology, Haifa, Israel.

Corresponding author: Avner Rothschild; Email: avner@mt.technion.ac.il

Abstract: Numerous studies have shown the addition of different impurities as dopants in hematite (α-Fe$_2$O$_3$) photoanodes improves the water photo-oxidation. The improvements observed may have resulted from electronic and/or catalytic effects, but also from changes in the layer morphology and microstructure induced by different precursors. The latter could be quite substantial, especially in mesoporous layers produced by chemical routes, making it difficult to make a systematic comparison between different dopants. This work attempts to overcome this difficulty by comparing different dopants in thin films produced by pulsed laser deposition (PLD), a physical deposition method that produces highly reproducible films with no significant variations in microstructure and morphology. This enables systematic comparison of the effect of different dopants without spurious side effects due to variations in microstructure and morphology. Thus, we examine the effect of Sn, Nb, Si, Pt, Zr, Ti, Zn, Ni and Mn dopants on the photoelectrochemical properties of thin (~50 nm) film hematite photoanodes deposited by PLD from Fe$_2$O$_3$ targets doped with ~1 cation% of the respective dopants onto FTO coated glass substrates. The morphology and microstructure of the films were nearly the same, independent of the different dopants in the films. The Sn-doped hematite photoanode outperformed all the other photoanodes that were

examined in this work in both the photocurrent and photovoltage, achieving the highest photocurrent (~ 1 mA/cm^2) and the lowest onset potential (~ 1.1 V$_{RHE}$). Based on a figure of merit that accounts for the maximum photocurrent $\times$ photovoltage product (i.e., power) as well as the potential at which the maximum power is achieved, our photoanodes ranked in the following order: Sn > Nb > Si > Pt > Zr > Ti > Zn > Ni > Mn. These observations are not always consistent with other reports on doped hematite photoanodes, suggesting that the photoelectrochemical properties and performance depend not only on the identity of the dopant but also on the dopant concentration, distribution and the morphology and microstructure of the photoanode in which the dopant is incorporated.

1. INTRODUCTION

Research on solar energy conversion and storage by means of photoelectrochemical (PEC) water splitting for renewable hydrogen production has intensively increased since the first demonstration of this effect by Fujishima and Honda [1]. Research in this field is motivated by the hope that PEC water splitting could potentially lead to a new technology for renewable production of hydrogen-based fuels as a sustainable alternative to fossil fuels [2]. The most critical challenge towards the development of this technology is, currently, the development of inexpensive, efficient, stable and durable photoanodes for water photo-oxidation. Among the prospective candidates, hematite (α–Fe$_2$O$_3$) is one of the most promising materials that could possibly meet these criteria. It is an abundant material, cheap, stable in alkaline solutions, a good catalyst for water oxidation [3], and it has a favorable energy band gap for tandem cells with Si PV cells [3,4]. Recent reports

on champion ultrathin (~20-30 nm) film [5] and mesoporous thick (400-500 nm) layer hematite photoanodes [6,7] achieved water photo-oxidation current densities (photocurrent for short) slightly above 4 mA/cm^2, which is still far below the theoretical limit of 12.6 mA/cm^2 for hematite under standard insolation (AM1.5G). Thus, despite the potential advantages and the remarkable progress in improving the performance of hematite photoanodes, there is still a long way to go in order to fulfill the expectations and meet the performance benchmarks for a viable PEC technology for solar water splitting using hematite photoanodes [8].

Several routes are being pursued in order to improve the performance of hematite photoanodes. The most successful ones include resonant light trapping in ultrathin films [5], nanostructuring of mesoporous thick layers [6,7], and employing underlayers and overlayers in order to enhance the charge separation and reduce surface recombination [9-12]. On top of these routes, which essentially tailor the device structure and morphology, there are other routes to improve the properties of the hematite itself. Most and foremost, doping is a powerful handle to tailor the charge carrier concentration as well as the catalytic properties of semiconductors in general and semiconducting metal-oxide photoelectrodes in particular. Indeed, doped hematite photoanodes generally perform much better than undoped ones [13,14]. While this is the general dogma in the field, there is a dispute among different researchers as for what are the "best" dopant and the optimal doping level (i.e., concentration). For instance, the Grätzel group employs Si as a dopant [6], whereas other groups including our group [5] as well as the Hamann [8], Vayssieres [15] and Barbier [16] groups use Ti. Other dopants that have been scrutinized recently by other research groups include Pt [7], Mn [17], Sn [18,19] Mg [20], Zr [21]

and Ni [22]. To the best of our knowledge, no systematic comparison (empirical comparison, excluding computational studies that were recently reviewed by Lia and Carter [23]) of the effect of different dopants on the photoelectrochemical performance of hematite photoanodes was reported in the last 3 decades, since the seminal investigation of Shinar and Kennedy [24]. Unfortunately, the latter work is a bit outdated, mainly because it centers on bulk materials, for the most part, whereas nowadays the focus is on mesoporous layers (thickness $\sim$ 500 nm) and ultrathin (< 50 nm) films. Thus, it is difficult to tell what dopants are more favorable than other ones for improving the performance of hematite photoanodes.

This work revisits this enigma and carries out a systematic empirical comparison between 9 different dopants (Si, Ti, Sn, Nb, Zr, Pt, Mn, Zn and Ni) in thin ($\sim$50 nm) film hematite photoanodes. The photoanodes are produced by pulsed laser deposition (PLD) from Fe_2O_3 targets doped with the respective dopants onto fluorinated tin oxide (FTO) coated glass substrates. Aiming for a systematic comparison wherein all the parameters are the same except for the impurity dopants, we selected PLD and this particular photoanode structure because it yields reproducible results [25]. Furthermore, the microstructure and morphology are nearly the same for all the photoanodes – independently of the different dopants, as shown in the following. This is crucial for systematic comparison of different dopants because the photoelectrochemical properties of hematite photoanodes are very sensitive to even small changes in microstructure and morphology that are often difficult to observe [6], so unless these parameters are kept unchanged it becomes very difficult to deconvolute between spurious microstructural and morphological effects and the "true" electronic and/or catalytic effects of the dopants. PLD enables precise control of the

chemical composition of the films with no influence on their microstructure and morphology, an enabling key for this study. In this work we examine the effect of different dopants at nominally the same concentration, ~1 cation%. In the near future we shall report the effect of different concentrations ("doping levels") for selected dopants.

2. EXPERIMENTAL

I. Synthesis of doped hematite photoanodes

(a) Substrates

Transparent conducting fluorinated tin oxide (F-doped SnO_2, FTO) coated soda-lime glass substrates (TEC15, Pilkington) were used throughout this work. Before deposition of the hematite films, the substrates were cleaned following the rigorous cleaning process described in [25]. This yields reproducible photoanodes as reported elsewhere [25].

(b) Targets

Doped hematite targets were prepared by solid state reaction of high purity powders of Fe_2O_3 (99.99% Alfa Aesar) and the following dopants: TiO_2, SiO_2, ZrO_2, SnO_2, Nb_2O_5, ZnO, NiO, MnO and PtO_2. The powders were mixed in appropriate amounts in order to obtain a cation concentration of 1% of the respective metal cation, M (i.e., $Fe_{1.98}M_{0.02}O_3$). The mixture was ball-milled for 24 h using YTZ milling balls (Tosoh, Japan), and subsequently pressed in a stainless steel mold and sintered in air at 1200°C for 12 h, resulting in a 1" disk-shaped pellet from which the films were deposited. The chemical composition of the targets was examined by EDS, and the results are presented in Table S1 (see supplementary information).

(c) Film deposition

Thin (~50 nm) films were deposited by PLD from the doped Fe_2O_3 targets onto clean TEC15 substrates. The deposition was carried out using a PLD system (2" PLD Workstation, Surface Systems & Technology) equipped with a KrF ($\lambda = 248$ nm) excimer laser (COMPexPro 102, Coherent). All the films were deposited using 9000 laser pulses with a fluence of 1 J/cm^2 and repetition rate of 3 Hz. The distance between the substrate and the target was 70 mm, and the heater set-point temperature was 500°C which corresponds to a substrate temperature of approximately 450°C. The deposition was carried out in O_2 gas atmosphere at a constant pressure of 25 mTorr.

II. Chemical and microstructural characterizations

The chemical composition of all the targets was examined by EDS (Oxford Instruments). In order to make sure that the film composition is the same as the composition of the respective target, we deposited thick (~1 μm) films from two of the targets (the Ti- and Nb-doped targets) and measured their chemical composition by EDS. The results are presented in Table S1 (see supplementary information). The surface morphology of all the films was examined by HRSEM with a field emission gun (Zeiss Ultra –Plus) under identical observation conditions. The phase composition of all the films was examined by XRD. X-ray diffractograms were acquired using an X-ray diffractometer (Rigaku SmatLab) in parallel beam configuration with Cu Kα radiation in the 2Θ range of 20-75° at a scan rate of 0.01°/s. The Scherrer domain size was calculated from the broadening of the hematite peaks using the Scherrer formula. The thickness of selected films was measured by cross-section TEM using a monochromated and aberration (image)

corrected TEM (FEI Titan 80-300 kV S/TEM). Cross-section TEM specimens were prepared by the lift out technique [26,27] using a dual-beam focused ion beam (FIB, FEI Strata 400S). High angle annular dark field (HAADF) micrographs and EDS composition maps were acquired in the STEM mode in order to examine the chemical composition across the hematite film and into the FTO layer.

III. Optical measurements

The optical properties of all the photoanodes were examined by spectrophotometry measurements in reflection and transmission modes using a spectrophotometer (Agilent Cary 5000) equipped with an integrating sphere.

IV. Photoelectrochemical measurements

The photoelectrochemical (PEC) measurements were carried out in an electrochemical cell known as the "cappuccino cell" [28] in three electrode configuration. The hematite photoanode served as the working electrode, a platinum wire served as the counter electrode, and an Ag/AgCl electrode in saturated KCl solution served as the reference electrode. The electrodes were immersed in 1M NaOH solution (pH = 13.6±0.1, measured by a pH meter, pH700 from EUTECH Instruments) inside the cappuccino cell. Current vs. potential linear sweep voltammograms were measured in the dark and under illumination at a potential ramp rate of 10 mV/s, and chopped light chronoamperometry measurements were carried out with 3 s exposure intervals. These measurements were carried out using a potentiostat (Ivium CompacStat) set in the three electrode mode configuration. The photoanodes were illuminated from the front side using a solar

simulator (ABET Technologies Sun 3000 class AAA solar simulator). Further details are provided elsewhere [25].

3. RESULT

Figure 1 shows HRSEM images of all the doped hematite films. The surface morphology is identical for all the films except for the Si-doped one that shows a fine granular morphology that was not observed in the rest of the films (see also high magnification HRSEM images in Figure S1 in the supplementary information). The surface morphology of the hematite films mimics that of the FTO coated glass substrates (see supplementary information Figure S2). This is indicative of conformal coverage of the hematite films on the substrates.
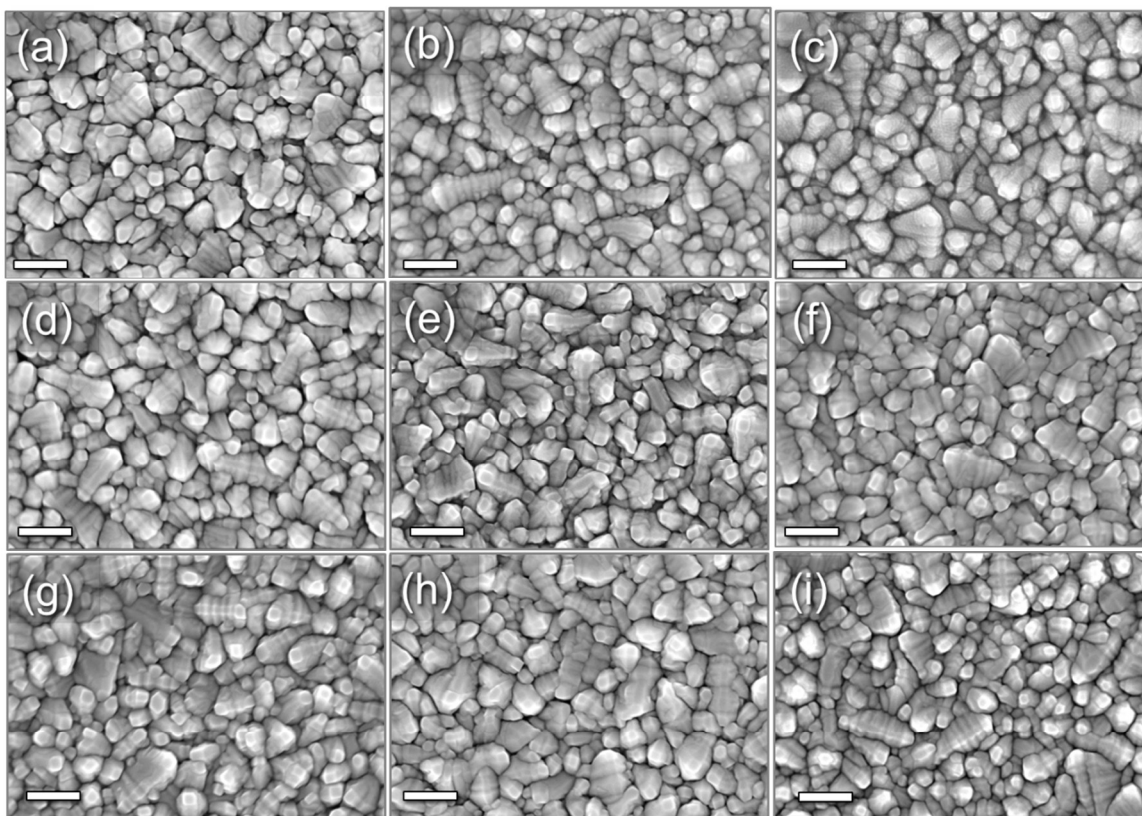
Figure 1. HRSEM images of hematite doped with (a) Sn, (b) Nb, (c) Si, (d) Pt, (e) Zr, (f) Ti, (g) Zn, (h) Ni, and (i) Mn. The scale bars correspond to 200 nm.

Figure 2 shows XRD diffractograms of all the photoanodes, as well as of an uncoated TEC15 substrate (for comparison). The labeled peaks correspond to Bragg reflections from the α-Fe$_2$O$_3$ hematite phase (JCPDS 01-080-5413) or from the SnO$_2$ rutile phase (JCPDS 01-079-6887). No other peaks are observed in the diffractograms. From the broadening of the α-Fe$_2$O$_3$ (110) peak we obtained a Scherrer domain size of ~10 nm for all the films (see supplementary information Table S2).
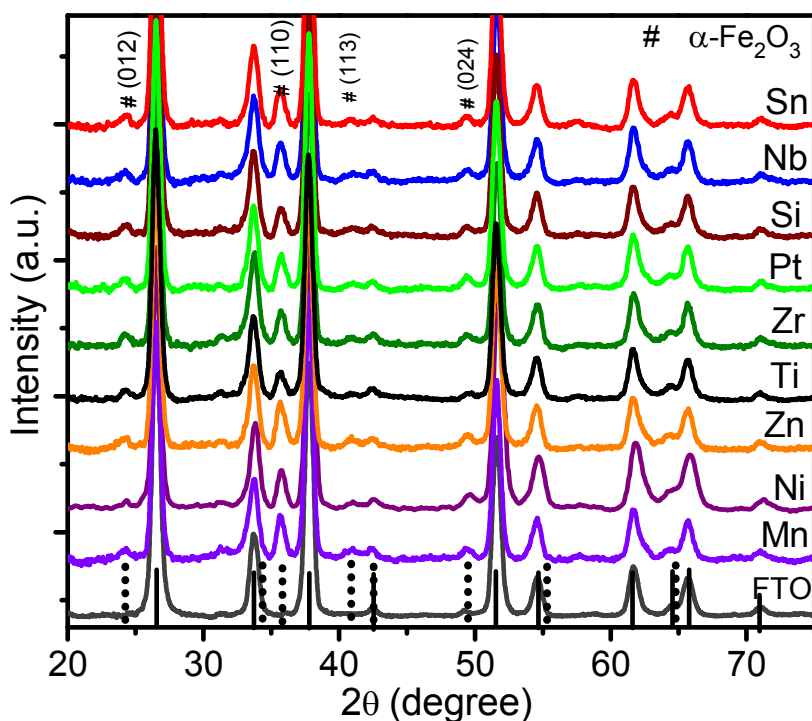

Figure 2. XRD diffractograms of doped hematite photoanodes. The respective dopants are shown on the right side of the respective plots. The α-Fe$_2$O$_3$ Bragg reflections are indexed at the top part of the figure. The 2Θ positions of Bragg reflections from the JCPDS files of α-Fe$_2$O$_3$ hematite (JCPDS 01-080-5413) and SnO$_2$ rutile (JCPDS 01-079-6887) are shown by the doted and full vertical lines, respectively, at the bottom of the figure.

Figure 3(a) shows a STEM-HAADF cross-section micrograph of a Sn-doped hematite film on an FTO-coated glass substrate (TEC15). The hematite film is coated with Pt and C layers, which is part of the TEM sample preparation. EDS elemental maps of the O K edge, Sn L edge and Fe K edge were taken from the area marked by the red rectangle and the results are shown in Figure 3(b). One can see that the hematite film covers the FTO-coated substrate conformably, with a film thickness of 48±5 nm. Other STEM-HAADF cross-section micrographs taken from the Ti-doped hematite film are shown in the supplementary information Figure S4. They show very similar characteristics as observed here for the Sn-doped hematite photoanode. Figure 3(c) shows HRTEM lattice image at the interface between the Sn-doped hematite film and the FTO layer. Note the sharp interface between the two layers.
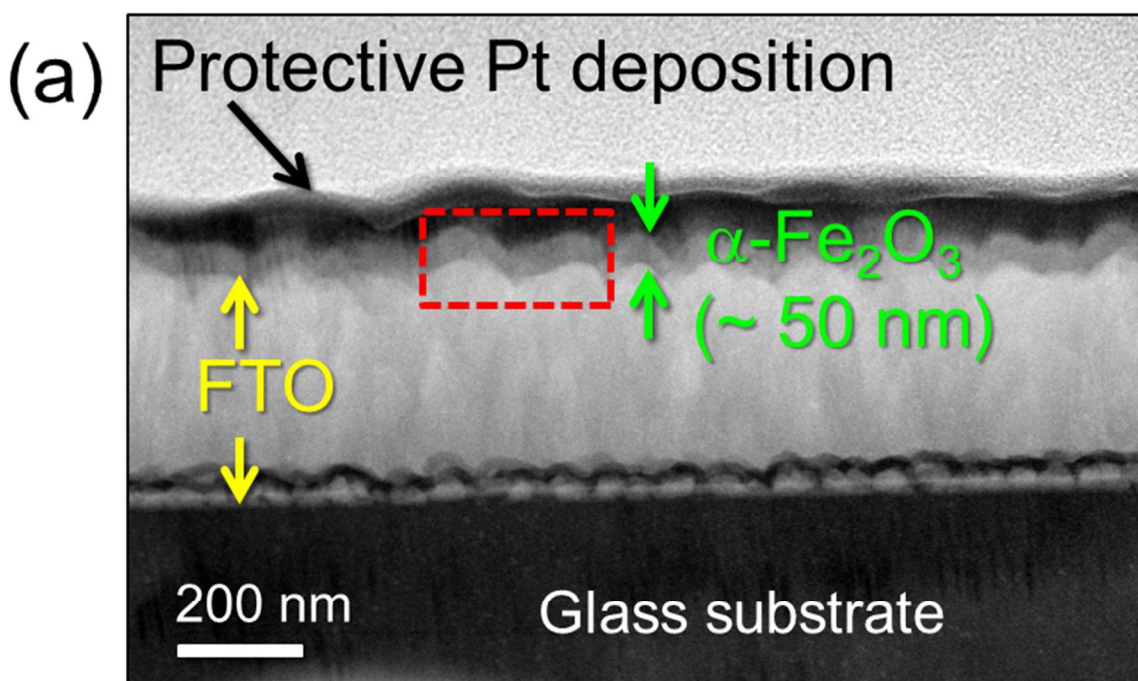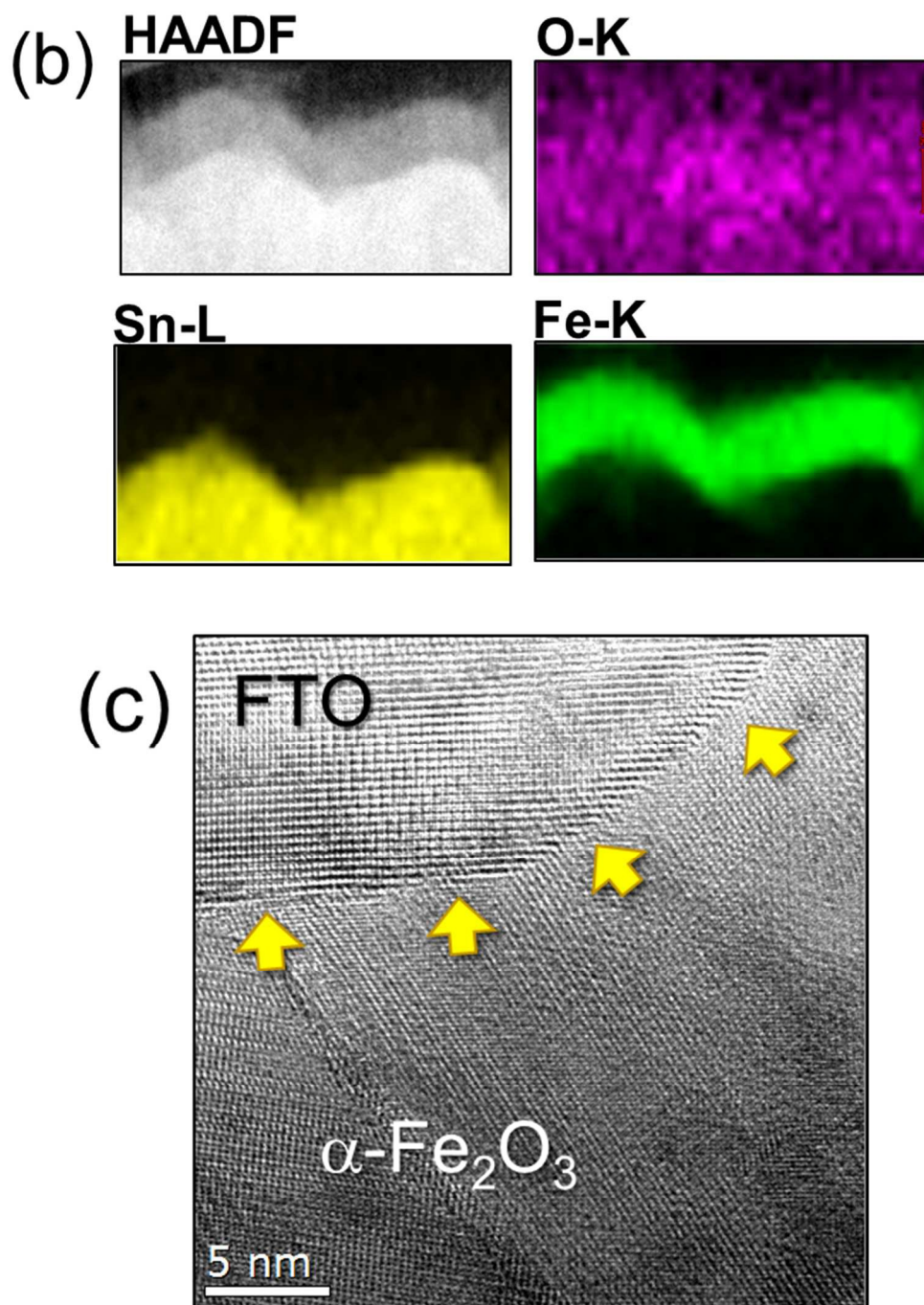
Figure 3. Cross-section micrographs of a Sn-doped hematite film on an FTO-coated glass substrate (TEC15): (a) STEM-HAADF image; (b) EDS elemental maps taken from the selected area (red box) in Fig. 3(a); and (c) HRTEM lattice image around the interface between hematite and FTO. Arrow shows the sharp interface between the two layers.

Shifting gears to the optical properties of the photoanodes, Figure 4 shows the absorptance spectra of all the photoanodes as well as of an uncoated TEC15 substrate. The absorptance was calculated using the formula $A = 1 - R - T$, where A and T are the reflectance and transmittance spectra (measured using an integrating sphere). The uncoated TEC15 substrate absorbs little above 350 nm and even more so above 400 nm. The absorption at shorter wavelengths in this specimen is due to band-to-band transition in the FTO. On the other hand, the hematite photoanodes absorb quite strongly down to 600 nm, the absorption edge of hematite (E_g = 2.1 eV), with a tail that extends up to 670 nm. At all wavelengths, except for the smallest ones (< 350 nm), the absorptance of the hematite photoanodes is much larger than that of the uncoated TEC15 substrate. It is noteworthy that the absorptance of all the hematite photoanodes is quite the same, except for the Ti-doped one that is smaller by ~4-8% than the other ones (see inset).
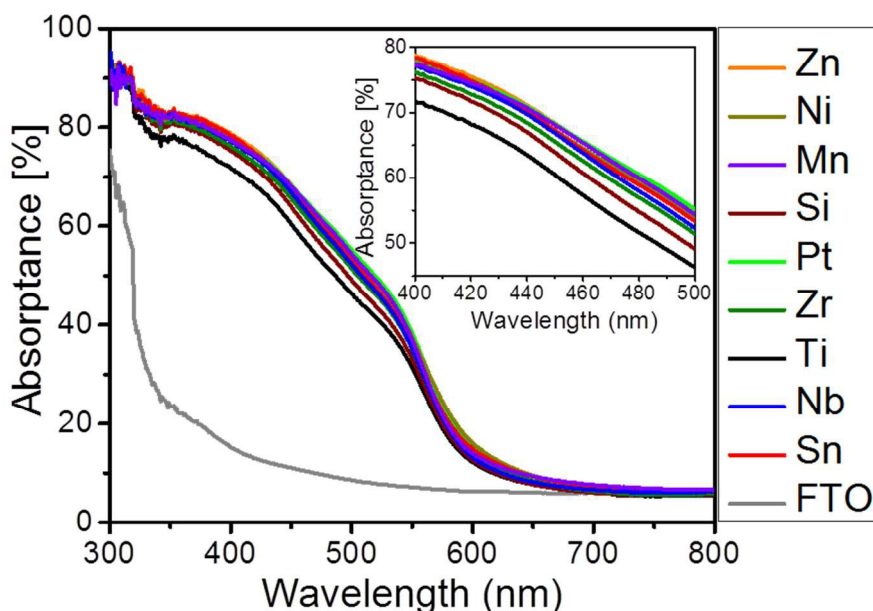

Figure 4. Absorptance spectra of all the photoanodes and an uncoated TEC15 substrate. The inset shows magnified view of spectra between 400 and 500 nm.

The flat band potential (U_{fb}) and dopant density (N_d) were obtained by Mott-Schottky analysis of capacitance vs. potential (*C-U*) measurements [29]. The analysis accounts for the Helmholtz capacitance (C_H) according to the following expression [30]:

$$\frac{1}{C^2} = \frac{2}{N_d e \varepsilon_r \varepsilon_0 A^2} \cdot \left[U_{fb} + U \right] + \frac{1}{C_H^2} \quad \dots (1)$$

where $\varepsilon_r = 33$ is the relative dielectric constant of hematite [31], ε_0 the permittivity of free space, *e* the elementary charge and *A* is the surface area of the photoanode exposed to the electrolyte. The surface area was taken as the exposed area of the photoanode within the cappuccino cell (0.28 cm^2) corrected by accounting for the surface roughness of the hematite films. AFM measurements showed that the roughness adds 4.6% to the nominal surface area (see supporting information Figure S4). The value of the Helmholtz capacitance used in the present analysis is $C_H = 10$ µF/cm^2. Figure 5(a) shows typical Mott-Schottky plots of the Sn-doped hematite photoanode measured at a frequency of 500 Hz in 1M NaOH solution with or without hole scavenger (0.5M H_2O_2) [32]. Both measurements yield the same results, confirming that the capacitance measured at this frequency is that of the space charge depletion region rather than that of the electrochemical reaction. Thus, the dopant densities were extracted from the slopes of the fitted straight lines (shown by the dash lines in Figure 5a) and the flat band potentials were obtained from the intercepts with the x-axis. Similar *C-U* plots were obtained also for the Ti, Zr, Pt, Si and Nb-doped hematite photoanodes, whereas the ones obtained for the Zn, Ni and Mn-doped hematite photoanodes had an odd shape that could not be fitted with straight lines as in Figure 5(a) (see supplementary information Figure S5).

Therefore, the Mott-Schottky analysis was applied only for the Sn, Ti, Zr, Pt, Si and Nb-doped hematite photoanodes and not for the Zn, Ni and Mn-doped ones. It is noteworthy that the former impurities (Sn, Ti, Zr, Pt, Si and Nb) behave as donor dopants whereas the latter ones (Zn, Ni and Mn) are not. Indeed, this was expected based on the lower oxidation state (+2) of the respective cations with respect to that of the cation they substitute (Fe^{+3}).   Figures 5(b) and (c) present the U_{fb} and N_d values obtained for the Sn, Ti, Zr, Pt, Si and Nb-doped hematite photoanodes by Mott-Schottky analysis of respective C-U measurements at different frequencies between 200 Hz and 25 kHz. Table S3 in the supplementary information lists all the frequencies at which the capacitance was measured. All the C-U measurements in this frequency range yielded Mott-Schottky plots with straight lines, as in Figure 5(a). The spread in the U_{fb} and N_d values in Figures 5(b) and (c) arises from C-U measurements at different frequencies. The flat band potentials were found to be between 0.3 and 0.7 V_{RHE} for all the photoanodes, and the dopant densities were of the order of $(0.6\text{-}1.6)\times10^{20}$ cm^{-3} except for the Ti-doped photoanode which was about 5 to 10 times higher than that.
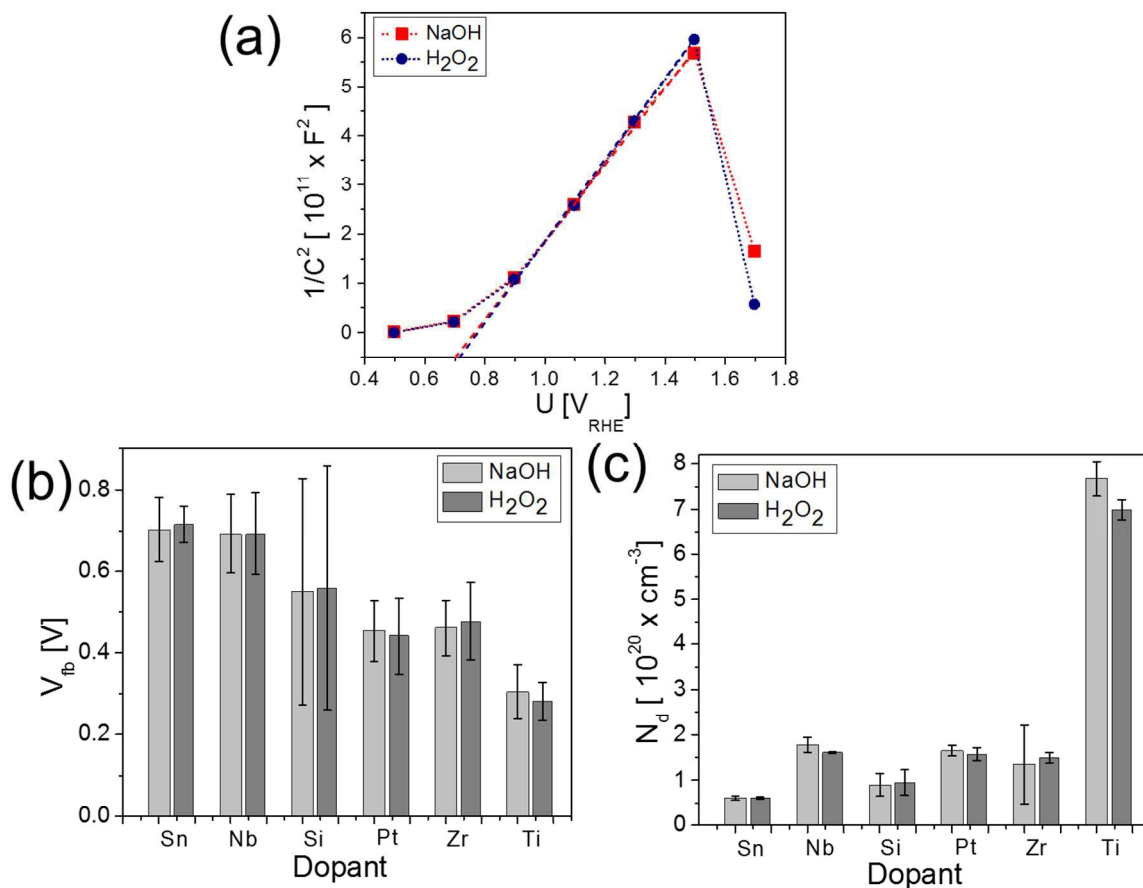
Figure 5. (a) Mott-Schottky plots of the Sn-doped hematite photoanode, measured at 500 Hz in 1M NaOH solution with and without 0.5M H_2O_2 (blue circles and red squares, respectively). (b) Flat band potentials; and (c) dopant densities obtained by Mott-Schottky analysis of C-U measurements carried out at different frequencies for the Sn, Ti, Zr, Pt, Si and Nb-doped hematite photoanodes.

Finally, the photoelectrochemical properties of all the photoanodes are shown in Figure 6. Figures 6(a) and (b) show light and dark voltammograms of all the photoanodes, measured in 1M NaOH solution. Figure 6(c) shows the respective photocurrent, that is the light minus dark currents, as a function of the photoanode potential. Complementary chopped-light chronoamperograms, as shown in the supplementary information Figure S6, display similar results to the linear-sweep light and dark voltammograms in Figures

6(a) and (b), respectively. This indicates that the linear-sweep voltammograms reflect the steady-state J-U behavior, both in the dark and under illumination. The highest photocurrents were obtained with the Sn-doped hematite photoanode, at all potentials. The lowest photocurrents were obtained with the Mn-doped hematite photoanode, at all potentials. In order to deconvolute between bulk and surface processes that limit the water photo-oxidation current we carried out light and dark voltammetry measurements in 1M NaOH solution with a hole scavenger (0.5M H_2O_2) [32]. The results are shown in Figure 6(d). Complementary chopped-light chronoamperograms are shown in the supplementary information Figure S7, displaying similar results to the linear-sweep light and dark voltammograms in Figure 6(d). With regards to the H_2O_2 measurements, the following observations are made: (1) The dark currents of all the photoanodes are similar, except for the Ni and Mn-doped photoanodes; (2) The Ni and Mn-doped hematite photoanodes show very little light currents; and (3) The Zn-doped hematite photoanode shows significantly higher light currents in the presence of H_2O_2 that without it. Last but not least, all the photoanodes were stable and they did not show any visible sign of decomposition following the PEC measurements (see photographs in the supplementary information Figure S8).
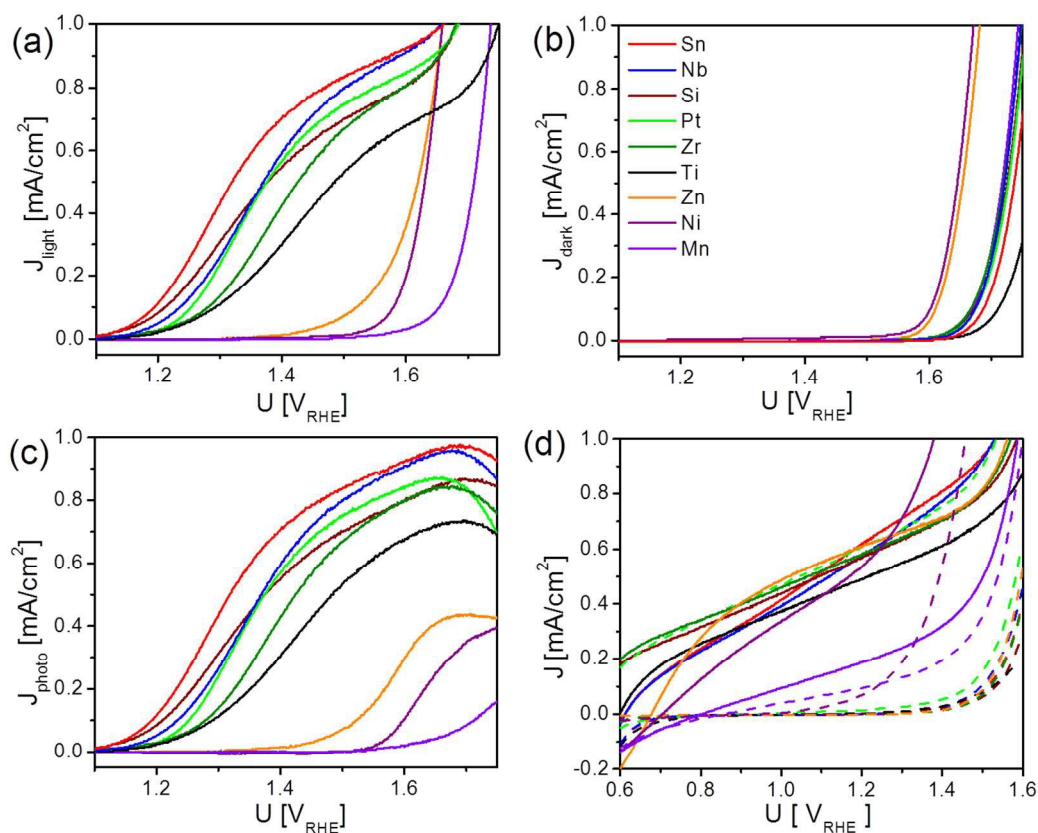
Figure 6. Light (a) and dark (b) voltammograms of all the photoanodes, measured in 1M NaOH solution. (c) Water photo-oxidation currents (i.e., photocurrents) of all the photoanodes, obtained by subtracting the respective dark currents from the light currents. (d) Light (full line curves) and dark (dashed line curves) voltammograms of all the photoanodes, measured in 1M NaOH solution with 0.5M H_2O_2. Different colors correspond to different dopants, as shown by the legend in Fig. (b).

4. DISCUSSION

The morphology and microstructure of all the photoanodes investigated in this work are nearly the same, independently of the dopants (see Figures 1 and 2), except for the Si-doped hematite film that has a fine granular surface morphology slightly different than the other films (see supplementary information Figure S1). The hematite films, ~50 nm

thick, coat the TEC15 substrates conformally, with no voids, cracks or pinholes (see Figure 3), and the interface between the hematite and FTO is sharp (see Figure 3c), showing no signs of solid state reaction between them. The dopant concentration in the targets is nearly the same for all targets (0.9 – 1.3 cation%), except for the Pt and Si-doped targets that have slightly smaller dopant concentrations (0.8 and 0.4 cation%, respectively) than the other ones. In general, PLD is known for nearly precise stoichiometry transfer from the target to the film [33]. This was verified in two of the photoanodes investigated in this work, the Ti and Nb-doped ones, by EDS measurements of thick (~1 µm) films deposited from the respective targets under the same conditions as the thin films. The Nb-doped hematite film has exactly the same chemical composition as that of the target from which it was deposited, whereas the Ti-doped hematite film has about half (more precisely, 60%) the amount of Ti than in the respective target (see supplementary information Table S1). This is probably due to the fact that unlike the other targets that were new and fresh, the Ti-doped Fe_2O_3 target is an old target that was already in service for several years before this study. Consequently, after hundreds of depositions it became very rough with a deep crater at the center, unlike the other targets that were flat and smooth. So all in all, we can confidently say that all the photoanodes, except for the Si-doped one, have the same morphology and microstructure, and they also have nearly the same dopant concentration, except for the Si and Ti-doped hematite photoanodes that have smaller dopant concentrations (about half) than the other ones. This provides a reasonable baseline for systematic comparison of the effect of different dopants on the PEC performance of thin film hematite photoanodes with nearly the same morphology, microstructure and dopant concentration.

In order to quantify the effect of the dopants on the PEC performance of the photoanodes, we use the following benchmarks: the maximum photocurrent, $J_{photo,max}$, and photocurrent values at the reversible and thermoneutral potentials of the water oxidation reaction (1.23 and 1.48 V_{RHE}, respectively), $J_{photo,@1.23V}$ and $J_{photo,@1.48V}$, respectively; and the rise-on potential, $U_{rise-on}$, defined as the potential at which the photocurrent reaches 0.1 mA/cm^2. The values of these benchmarks are extracted directly from Figure 6(c), as shown in Figure 7(a) for the case of the Sn-doped hematite photoanode. On top of these conventional benchmarks, we add another one: the figure of merit (*FOM*), defined here as the maximum solar to chemical conversion efficiency, $ISTC_{max}$, divided by the potential (under light) at which it is reached, $U_{light}(ISTC_{max})$, normalized by the reversible potential of the water oxidation reaction (1.23 V_{RHE}), that is:

$$FOM = \frac{ISTC_{max}}{U_{light}(ISTC_{max})/1.23[V_{RHE}]} . \quad (2)$$

The *ISTC* is calculated as per the following formula [34]:

$$ISTC = \frac{1.23(V_{RHE})}{U_{dark}(V_{RHE})}\left[\frac{J_{photo}V_{photo}}{P_{solar}}\right]_{AM1.5G} \quad (3)$$

where V_{photo} is the photovoltage, defined as the difference between the dark and light potentials at the same current density, i.e., $V_{photo}(J) = U_{dark}(J) - U_{light}(J)$, J_{photo} is the photocurrent density, U_{dark} is the potential at which J is reached in the dark, and $P_{solar} = 100$ mW/cm^2 is the power density of the solar simulated radiation (AM1.5G). Figure 7(a) shows how V_{photo} and J_{photo} are obtained at one point ($J = 0.7$ mA/cm^2) on the voltammograms of the Sn-doped hematite photoanode. Figures 7(b) and (c) show the

J$_{photo}$ vs. *V$_{photo}$* and *ISTC* vs. *J$_{photo}$* curves obtained for this photoanode from the results in Figure 7(a). From the *ISTC* curve (Figure 7(c)) we obtain the *ISTC$_{max}$* and *U$_{light}$*(*ISTC$_{max}$*) values, 0.18% and 1.4 V$_{RHE}$, respectively. Thus, the *FOM* of the Sn-doped hematite photoanode is 0.16%. Similar calculations were made for all the photoanodes, except for the Ni and Mn doped ones for which the low photocurrents resulted in large errors in the analysis. The results are summarized in Figures 7(d) *J$_{photo,max}$*, (e) *J$_{photo,@1.23V}$*, (f) *J$_{photo,@1.48V}$*, (g) *U$_{rise-on}$*, (h) *V$_{photo,max}$* (maximum photovoltage), and (i) *FOM*.
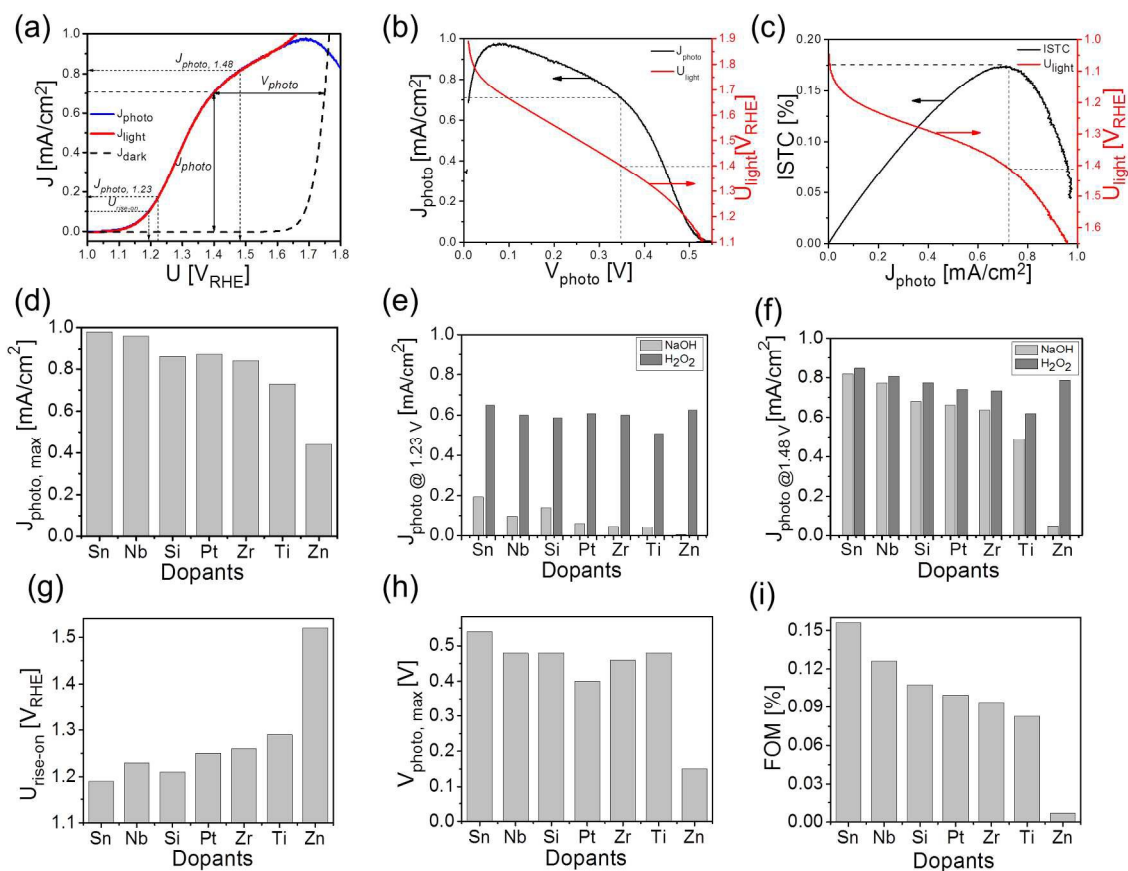

Figure 7. (a) Shows current density vs. applied potential for Sn-doped hematite photoanode with the characteristics parameters in the plot. (b-c) shows the method to calculate *J$_{photo}$*, *V$_{photo}$* and *ISTC* with respect to the applied potential (*U*). The defined parameters for all doped photoanodes were plotted in histograms as (d) *J$_{photo,max}$*, (e) *J$_{photo,@1.23V}$*, (f) *J$_{photo,@1.48V}$*, (g) *U$_{rise-on}$*, (h) *V$_{photo,max}$* and (i) *FOM*.

Among all the photoanodes examined in this work, the Sn-doped one achieved the highest scores in all the benchmarks, reaching the highest photocurrents at all potentials, with the lowest onset and rise-on potentials and the highest photovoltages, and reaching the highest figure of merit. Looking only at the photocurrent, the ranking order is Sn > Nb > (Si, Pt, Zr) > Ti >> Zn >> Ni >> Mn (see also Figure 6c). Looking only at the (maximum) photovoltage, the ranking order is Sn > (Nb, Si, Ti, Zr) > Pt >> Zn, with no data available for the Ni and Mn-doped photoanodes. The combined ranking order that takes into account both the photocurrent and the photovoltages, that is the figure of merit (FOM), yields Sn > Nb > Si > Pt > Zr > Ti >> Zn, with no data available for the Ni and Mn-doped photoanodes. It is noteworthy that the Zn-doped hematite photoanode displayed low photocurrents for water oxidation, but the photocurrents in the presence of hole scavenger (H_2O_2) were quite high, comparable to the other photoanodes. The main weakness of this photoanode was low photovoltage and high onset and rise-on potentials for water photo-oxidation.

Comparison with previous reports on hematite photoanodes shows that these results are not always consistent with other reports. For instance, here we find the Mn-doped hematite photoanode to underperform with respect to all the other photoanodes examined in this work, whereas other researchers report Mn-doped hematite photoanodes to give rise to quite high photocurrents [17]. The discrepancy is most likely due to the markedly different morphology, microstructure and Mn concentration between the respective photoanodes. Thus, at this point all we can say is that our observations and the benchmarking comparison in Figure 7 hold for the photoanodes examined in this work, but not necessarily for other hematite photoanodes with different morphology,

microstructure and dopant concentrations. It appears that the PEC properties and performance of the photoanode depend not only on the identity of the dopant but also on its concentration, distribution and on the morphology and microstructure of the photoanode in which it is incorporated, rendering a comparative study of the effect of different dopants quite a challenging endeavor.

5. CONCLUSIONS

The effect of Sn, Nb, Si, Pt, Zr, Ti, Zn, Ni and Mn dopants on the PEC properties of thin (~50 nm) film hematite photoanodes was examined. The doped hematite films were deposited by PLD from Fe_2O_3 targets doped with ~1 cation% of the respective dopants onto FTO coated glass substrates. The morphology and microstructure of the films were nearly the same, independent of the different dopants in the films. The Sn-doped hematite photoanode outperformed all the other photoanodes that were examined in this work in both the photocurrent and photovoltage, achieving the highest photocurrent (~1 mA/cm^2) and lowest onset potential (~1.1 V$_{RHE}$). Based on a figure of merit that accounts for the maximum photocurrent $\times$ photovoltage product (i.e., power) as well as the potential at which the maximum power is achieved, our photoanodes ranked in the following order: Sn > Nb > Si > Pt > Zr > Ti > Zn > Ni > Mn. These observations are not always consistent with other reports on doped hematite photoanodes produced by other researchers, suggesting that the PEC properties and performance of the photoanode depend not only on the identity of the dopant but also on its concentration, distribution and on the morphology and microstructure of the photoanode in which it is incorporated.

ACKONWLEDGEMENT

References

[1] Fujishima A, Honda K. Electrochemical Photolysis of Water at a Semiconductor Electrode. Nature 1972;238:37-8.

[2] Lewis NS, Nocera DG. Powering the planet: Chemical challenges in solar energy utilization. Proceedings of the National Academy of Sciences 2006;103:15729-35.

[3] Sivula K, Le Formal F, Grätzel M. Solar Water Splitting: Progress Using Hematite (α-Fe_2O_3) Photoelectrodes. ChemSusChem 2011;4:432-49.

[4] Smith RDL, Prévot MS, Fagan RD, Zhang Z, Sedach PA, Siu MKJ, et al. Photochemical Route for Accessing Amorphous Metal Oxide Materials for Water Oxidation Catalysis. Science 2013;340:60-3.

[5] Dotan H, Kfir O, Sharlin E, Blank O, Gross M, Dumchin I, et al. Resonant light trapping in ultrathin films for water splitting. Nat Mater 2013;12:158-64.

[6] Warren SC, Voïtchovsky K, Dotan H, Leroy CM, Cornuz M, Stellacci F, et al. Identifying champion nanostructures for solar water-splitting. Nat Mater 2013;12:842-9.

[7] Kim JY, Magesh G, Youn DH, Jang J-W, Kubota J, Domen K, et al. Single-crystalline, wormlike hematite photoanodes for efficient solar water splitting. Scientific Reports 2013;3:2681.

[8] Zandi O, Hamann TW. The potential versus current state of water splitting with hematite. Physical Chemistry Chemical Physics 2015;17:22485-503.

[9] Hisatomi T, Dotan H, Stefik M, Sivula K, Rothschild A, Grätzel M, et al. Enhancement in the Performance of Ultrathin Hematite Photoanode for Water Splitting by an Oxide Underlayer. Advanced Materials 2012;24:2699-702.

[10] Barroso M, Cowan AJ, Pendlebury SR, Grätzel M, Klug DR, Durrant JR. The Role of Cobalt Phosphate in Enhancing the Photocatalytic Activity of α-Fe_2O_3 toward Water Oxidation. Journal of the American Chemical Society 2011;133:14868-71.

[11] Du C, Yang X, Mayer MT, Hoyt H, Xie J, McMahon G, et al. Hematite-Based Water Splitting with Low Turn-On Voltages. Angewandte Chemie International Edition 2013;52:12692-5.

[12] Tilley SD, Cornuz M, Sivula K, Grätzel M. Light-Induced Water Splitting with Hematite: Improved Nanostructure and Iridium Oxide Catalysis. Angewandte Chemie International Edition 2010;49:6405-8.

[13] Glasscock JA, Barnes PRF, Plumb IC, Savvides N. Enhancement of Photoelectrochemical Hydrogen Production from Hematite Thin Films by the Introduction of Ti and Si. The Journal of Physical Chemistry C 2007;111:16477-88.

[14] Zandi O, Klahr BM, Hamann TW. Highly photoactive Ti-doped α-Fe$_2$O$_3$ thin film electrodes: resurrection of the dead layer. Energy & Environmental Science 2013;6:634-42.

[15] Kronawitter CX, Zegkinoglou I, Shen SH, Liao P, Cho IS, Zandi O, et al. Titanium incorporation into hematite photoelectrodes: theoretical considerations and experimental observations. Energy & Environmental Science 2014;7:3100-21.

[16] Rioult M, Magnan H, Stanescu D, Barbier A. Single Crystalline Hematite Films for Solar Water Splitting: Ti-Doping and Thickness Effects. The Journal of Physical Chemistry C 2014;118:3007-14.

[17] Gurudayal, Chiam SY, Kumar MH, Bassi PS, Seng HL, Barber J, et al. Improving the Efficiency of Hematite Nanorods for Photoelectrochemical Water Splitting by Doping with Manganese. ACS Applied Materials & Interfaces 2014;6:5852-9.

[18] Ling Y, Wang G, Wheeler DA, Zhang JZ, Li Y. Sn-Doped Hematite Nanostructures for Photoelectrochemical Water Splitting. Nano Letters 2011;11:2119-25.

[19] Bohn CD, Agrawal AK, Walter EC, Vaudin MD, Herzing AA, Haney PM, et al. Effect of Tin Doping on α-Fe$_2$O$_3$ Photoanodes for Water Splitting. The Journal of Physical Chemistry C 2012;116:15290-6.

[20] Lin Y, Xu Y, Mayer MT, Simpson ZI, McMahon G, Zhou S, et al. Growth of p-Type Hematite by Atomic Layer Deposition and Its Utilization for Improved Solar Water Splitting. Journal of the American Chemical Society 2012;134:5508-11.

[21] Shen S, Guo P, Wheeler DA, Jiang J, Lindley SA, Kronawitter CX, et al. Physical and photoelectrochemical properties of Zr-doped hematite nanorod arrays. Nanoscale 2013;5:9867-74.

[22] Liu Y, Yu Y-X, Zhang W-D. Photoelectrochemical properties of Ni-doped Fe_2O_3 thin films prepared by electrodeposition. Electrochimica Acta 2012;59:121-7.

[23] Liao P, Carter EA. New concepts and modeling strategies to design and evaluate photo-electro-catalysts based on transition metal oxides. Chemical Society Reviews 2013;42:2401-22.

[24] Shinar R, Kennedy JH. Photoactivity of doped α-Fe_2O_3 electrodes. Solar Energy Materials 1982;6:323-35.

[25] Malviya KD, Dotan H, Yoon KR, Kim I-D, Rothschild A. Rigorous substrate cleaning process for reproducible thin film hematite (α-Fe_2O_3) photoanodes. Journal of Materials Research 2015;FirstView:1-9.

[26] Sivel VGM, Van Den Brand J, Wang WR, Mohdadi H, Tichelaar FD, Alkemade PFA, et al. Application of the dual-beam FIB/SEM to metals research. Journal of Microscopy 2004;214:237-45.

[27] Steve R, Robert P. A review of focused ion beam applications in microsystem technology. Journal of Micromechanics and Microengineering 2001;11:287.

[28] Krol Rvd. Principles of Photoelectrochemical Cells. In: Roel van de Krol MG, editor. Photoelectrochemical Hydrogen Production: Springer 2012. p. 13-67.

[29] Gelderman K, Lee L, Donne SW. Flat-Band Potential of a Semiconductor: Using the Mott–Schottky Equation. Journal of Chemical Education 2007;84:685.

[30] Francisco Fabregat-Santiagoa GG-B, Juan Bisquerta, Peter Bogdanoffb and Arie Zabanc,. Mott-Schottky Analysis of Nanoporous Semiconductor Electrodes in Dielectric State Deposited on $SnO_2(F)$ Conducting Substrates. J Electrochem Soc 2003;150:293-8.

[31] Lunt RA, Jackson AJ, Walsh A. Dielectric response of Fe_2O_3 crystals and thin films. Chemical Physics Letters 2013;586:67-9.

[32] Dotan H, Sivula K, Gratzel M, Rothschild A, Warren SC. Probing the photoelectrochemical properties of hematite (α-Fe_2O_3) electrodes using hydrogen peroxide as a hole scavenger. Energy & Environmental Science 2011;4:958-64.

[33] Douglas B. Chrisey GKH. Pulsed Laser Deposition of Thin Films. New York: John Wiley and Sons, Inc.; 1994.

[34] Dotan H, Mathews N, Hisatomi T, Grätzel M, Rothschild A. On the Solar to Hydrogen Conversion Efficiency of Photoelectrodes for Water Splitting. The Journal of Physical Chemistry Letters 2014;5:3330-4.